Disorder effects in correlated topological insulators

Hsiang-Hsuan Hung, Aaron Barr, Emil Prodan, and Gregory A. Fiete

Phys. Rev. B **94**, 235132 — Published 13 December 2016

DOI: 10.1103/PhysRevB.94.235132

Disorder effects in correlated topological insulators

Hsiang-Hsuan Hung,[1] Aaron Barr,[1] Emil Prodan,[2] and Gregory A. Fiete[1]

[1] *Department of Physics, The University of Texas at Austin, Austin, TX, 78712, USA*
[2] *Department of Physics, Yeshiva University, New York, NY, 10016, USA*

(Dated: November 28, 2016)

Using exact diagonalization and quantum Monte Carlo calculations we investigate the effects of disorder on the phase diagram of both non-interacting and interacting models of two-dimensional topological insulators. In the fermion sign problem-free interacting models we study, electron-electron interactions are described by an on-site repulsive Hubbard interaction and disorder is included via the one-body hopping operators. In both the non-interacting and interacting models we make use of recent advances in highly accurate real-space numerical evaluation of topological invariants to compute phase boundaries, and in the non-interacting models determine critical exponents of the transitions. We find different models exhibit distinct stability conditions of the topological phase with respect to interactions and disorder. We provide a general analytical theory that accurately predicts these trends.

PACS numbers: 71.10.Fd,71.70.Ej

I. INTRODUCTION

Topological insulators have emerged as a topic of intense research focus[1–4]. When electron-electron interactions are an essential ingredient of a topological phase, the phenomenology is remarkably richer, though the full range of possible behaviors is not yet fully understood[5–9]. A topic that has thus far received comparatively little attention is the influence of disorder on interacting topological phases. For non-interacting topological insulators, there has been a flurry of activity around the topological Anderson insulator (TAI), which results from random terms in the Hamiltonian that drive a non-topological system into a topological state[10,11,16–18,46–49]. However, even in non-topological systems the combination of disorder and interactions is known to be a particularly challenging problem[19–23].

In this work we focus on disordered variants of the two-dimensional Kane-Mele (KM) model[43,44], selected because they do not have a fermion sign problem when simulated with quantum Monte Carlo (QMC)[41,42] provided the disorder is on the hopping terms[28,46] (bond disorder) of the model rather than the on-site chemical potential[47–49] (because particle-hole symmetry is preserved in the former case). These models allow one to investigate the combination of disorder and interactions in a topological system with a high degree of numerical accuracy, especially when combined[?] with recent advances in the real-space numerical evaluation of topological invariants[39], as we use in this work.

In the limiting case of weak disorder and interactions, we also present an analytical theory that accurately describes the interplay of disorder and interactions near the phase boundary between the topological and trivial phases of the models. The generality of the analytical theory suggests that it should correctly predict trends in other two and three dimensional models as well, regardless of whether they have a fermion sign problem. This may open the door to wider studies of disorder in interacting topological phases, at least for certain regimes of the parameter space. A central result of this work is that the physics of disorder in topological phases depends crucially on the momentum values of gap closing points in the clean limit. We illustrate this explicitly with our models, which exhibit a different behavior with respect to disorder from those studied previously.

Before turning to the study of interacting models, we first contrast bond and on-site disorder in the non-interacting limit of these models using large scale exact diagonalization and highly accurate real-space evaluation of topological invariants of finite-size systems. Our computations, combined with a finite-size scaling analysis, allow a precise determination of phase boundaries, as well as the critical exponents of the transition, which agree with general theoretical expectations based on the symmetry classes of the models.

The main results of this work are: (1) The identification of a new class of disordered, interacting, topological models that can be solved numerically exactly with fermion sign-problem free quantum Monte Carlo calculations, (2) The accurate evaluation of critical exponents in this model, made possible by recent advances in real-space formulas for the numerical evaluation of topological invariants, (3) The presentation of a general, model-independent combined mean-field/perturbation theory approach that allows one to study the effects of disorder and interactions quasi-analytically in certain regimes of the parameter space, and (4) The physical result that the most common classes of disorder (on-site and hopping) tend to stabilize topological phases in these models even when interactions are included.

Our paper is organized as follows. In Sec. II we describe the generalized versions of the Kane-Mele Hamiltonian we study in this work. In Sec.III we detail the real-space formalism we use to evaluate the topological invariants for the disordered systems we consider, and in Sec.IV we show the numerical results. In Sec.V we detail the self-consistent Born approximation, a semi-analytic

method, that we used to treat both disorder and interaction effects simultaneously, the numerical results of which are presented in Sec.VI. Finally, in Sec.VII we present the main conclusions of this work.

II. MODEL HAMILTONIANS

A. The KM Model

We study two variants of the well-known KM model[43,44] (and the KM model itself),

$$H_{\rm KM} = -\sum_{\langle i,j\rangle,\sigma} c^\dagger_{i\sigma} c_{j\sigma} + i\lambda_{SO} \sum_{\langle\langle i,j\rangle\rangle,\sigma} \sigma c^\dagger_{i\sigma} \nu_{ij} c_{j\sigma}, \quad (1)$$

defined on the honeycomb lattice where $\langle\cdots\rangle$ runs over nearest-neighbor sites and $\langle\langle\cdots\rangle\rangle$ over next-nearest-neighbor sites, and $\sigma = \pm 1$ describes the spin projection along the z-axis. The operator $c_{i\sigma}$ annihilates a fermion on site i, and $c^\dagger_{i\sigma}$ creates a fermion on site i. Each unit cell contains two sites, labeled as A and B. The spin-orbit coupling strength is λ_{SO}, and $\nu_{ij} = +1$ for counter-clockwise hopping along a hexagonal plaquette and $\nu_{ij} = -1$ for clockwise hopping[?] .

In the absence of Rashba potential, the KM model preserves the z-projection of the spin, hence it may be regarded as two "copies" of the Haldane model[30], with

$$H_\uparrow = -\sum_{\langle i,j\rangle} c^\dagger_{i\uparrow} c_{j\uparrow} + i\lambda_{SO} \sum_{\langle\langle i,j\rangle\rangle} c^\dagger_{i\uparrow} \nu_{ij} c_{j\uparrow}, \quad (2)$$

for the spin up component and its time-reversed partner for the spin-down component. For any non-zero value of λ_{SO}, each spin projection has been shown to be a quantum Hall (QH) insulator[30] with opposite Chern numbers, Ch $= \pm 1$, for the two spin projections. Likewise, the KM model is in the Z_2 topologically non-trivial phase when λ_{SO} is non-zero. Therefore, the Hamiltonian in Eq.(1) will be regarded as a "parent Hamiltonian" to which we will add an on-site Hubbard interaction, $H_U = U\sum_i n_{i\uparrow} n_{i\downarrow}$, other spin-independent hopping terms, and various sources of disorder (both bond disorder and on-site disorder in the non-interacting limit). Taking advantage of the conservation of the z-component of the spin, much of our analysis of the topological properties will be focused on computing the Chern numbers of the spin sectors[31–33] as a function of model parameters.

B. The GKM Model

Here we provide the Hamiltonian expression for the GKM model[41,42] (generalization of the well-known Kane-Mele model[43,44]), and develop its effective low-energy theory. The GKM model is given by $H_{\rm GKM} = H_{\rm KM} + H_{t_3}$, where $H_{t_3} = -t_3 \sum_{\langle\langle\langle i,j\rangle\rangle\rangle,\sigma} c^\dagger_{i\sigma} c_{j\sigma}$ where $\langle\langle\langle\cdots\rangle\rangle\rangle$ runs over third-nearest-neighbor sites. It can be expressed in momentum space as[74],

$$H_{GKM} = \sum_{\mathbf{k}\in B.Z.} \Psi^\dagger_{\mathbf{k}} \left[\begin{pmatrix} 0 & -tf(\mathbf{k}) - t_3 f_3(\mathbf{k}) \\ -tf^*(\mathbf{k}) - t_3 f_3^*(\mathbf{k}) & 0 \end{pmatrix} \otimes \mathbb{1}_{2\times 2} + \begin{pmatrix} 2\lambda_{so} g(\mathbf{k}) & 0 \\ 0 & -2\lambda_{so} g(\mathbf{k}) \end{pmatrix} \otimes \sigma_z \right] \Psi_{\mathbf{k}}, \quad (3)$$

where the basis $\Psi^T_{\mathbf{k}} \equiv (\Psi^{\uparrow T}_{\mathbf{k}} \quad \Psi^{\downarrow T}_{\mathbf{k}}) = (c_{\mathbf{k}\uparrow}(A) \quad c_{\mathbf{k}\uparrow}(B) \quad c_{\mathbf{k}\downarrow}(A) \quad c_{\mathbf{k}\downarrow}(B))$ with $\mathbf{k}$ denoting the momentum, $\uparrow,\downarrow$ the z-axis projections of the spin, and A, B the sub lattice degrees of freedom shown in Fig. 1(a). Here σ_z is the Pauli matrix for the spin degrees of freedom. The expressions $g(\mathbf{k}) \equiv -\sin(\mathbf{k}\cdot\mathbf{e}_1) + \sin(\mathbf{k}\cdot\mathbf{e}_2) + \sin[\mathbf{k}\cdot(\mathbf{e}_1 - \mathbf{e}_2)]$, $f(\mathbf{k}) = 1 + e^{i\mathbf{k}\cdot\mathbf{e}_1} + e^{i\mathbf{k}\cdot\mathbf{e}_2}$ and $f_3(\mathbf{k}) = e^{i\mathbf{k}\cdot(\mathbf{e}_1+\mathbf{e}_2)} + 2\cos[\mathbf{k}\cdot(\mathbf{e}_1 - \mathbf{e}_2)]$, where $\mathbf{e}_1 = (1/2, \sqrt{3}/2)$ and $\mathbf{e}_2 = (-1/2, \sqrt{3}/2)$.

The B.Z. is shown in Fig. 1(b). In the KM-type models that we consider, a few momenta dominate the low-energy descriptions[74]. As a function of t_3, gap closings occur at the TRIM points located at $\mathbf{M}_{1,2} \equiv (\pm\pi, \pi/\sqrt{3})$ and $\mathbf{M}_3 \equiv (0, 2\pi/\sqrt{3})$. At the TRIM, the diagonal elements of the Hamiltonian matrices vanish, $g(\mathbf{M}_a) = 0$, and the band gaps in GKM are controlled by the off-diagonal elements, which are related to real-valued first and third neighbor hopping. The low-energy form (to quadratic order in the momentum, needed for the self-consistent Born approximation in the case of disorder) of the Hamiltonian near the three different $\mathbf{M}_a$ can be

obtained by expanding $f(\mathbf{k})$, $f_3(\mathbf{k})$, and $g(\mathbf{k})$ as

$$f(\mathbf{M_1}+\delta\mathbf{k}) = 1 - i\delta k_x + \frac{\sqrt{3}}{2}\delta k_x \delta k_y, \tag{4}$$

$$f_3(\mathbf{M_1}+\delta\mathbf{k}) = -3 - i\sqrt{3}\delta k_y + \frac{3}{2}\delta k_y^2 + \delta k_x^2, \tag{5}$$

$$g(\mathbf{M_1}+\delta\mathbf{k}) = \sqrt{3}\delta k_y - \delta k_x, \tag{6}$$

$$f(\mathbf{M_2}+\delta\mathbf{k}) = 1 + i\delta k_x - \frac{\sqrt{3}}{2}\delta k_x \delta k_y, \tag{7}$$

$$f_3(\mathbf{M_2}+\delta\mathbf{k}) = -3 - i\sqrt{3}\delta k_y + \frac{3}{2}\delta k_y^2 + \delta k_x^2, \tag{8}$$

$$g(\mathbf{M_2}+\delta\mathbf{k}) = -\sqrt{3}\delta k_y - \delta k_x \tag{9}$$

$$f(\mathbf{M_3}+\delta\mathbf{k}) = -1 - i\sqrt{3}\delta k_y + \frac{3}{4}\delta k_y^2 + \frac{1}{4}\delta k_x^2, \tag{10}$$

$$f_3(\mathbf{M_3}+\delta\mathbf{k}) = 3 + i\sqrt{3}\delta k_y - \frac{3}{2}\delta k_y^2 - \delta k_x^2, \tag{11}$$

$$g(\mathbf{M_3}+\delta\mathbf{k}) = 2\delta k_x. \tag{12}$$

The low-energy forms of the GKM model for the various $\mathbf{M}_a$ points are given by

$$H^{eff}_{GKM}(\mathbf{M_1}+\delta\mathbf{k}) = \begin{pmatrix} 2\sqrt{3}\lambda\delta k_y - 2\lambda\delta k_x & -t+3t_3 + i(\sqrt{3}t_3\delta k_y + t\delta k_x) + p_1(\delta\mathbf{k}) \\ -t+3t_3 - i(\sqrt{3}t_3\delta k_y + t\delta k_x) + p_1(\delta\mathbf{k}) & -2\sqrt{3}\lambda\delta k_y + 2\lambda\delta k_x \end{pmatrix}, \tag{13}$$

$$H^{eff}_{GKM}(\mathbf{M_2}+\delta\mathbf{k}) = \begin{pmatrix} -2\sqrt{3}\lambda\delta k_y - 2\lambda\delta k_x & -t+3t_3 + i(\sqrt{3}t_3\delta k_y - t\delta k_x) + p_2(\delta\mathbf{k}) \\ -t+3t_3 - i(\sqrt{3}t_3\delta k_y - t\delta k_x) + p_2(\delta\mathbf{k}) & 2\sqrt{3}\lambda\delta k_y + 2\lambda\delta k_x \end{pmatrix}, \tag{14}$$

$$H^{eff}_{GKM}(\mathbf{M_3}+\delta\mathbf{k}) = \begin{pmatrix} 4\lambda\delta k_x & t-3t_3 + i\sqrt{3}(t-t_3)\delta k_y + p_3(\delta\mathbf{k}) \\ t-3t_3 - i\sqrt{3}(t-t_3)\delta k_y + p_3(\delta\mathbf{k}) & -4\lambda\delta k_x \end{pmatrix}, \tag{15}$$

where $p_1(\delta\mathbf{k}) = -\frac{3}{2}t_3\delta k_y^2 - \frac{\sqrt{3}}{2}t\delta k_y\delta k_x - t_3\delta k_x^2$, $p_2(\delta\mathbf{k}) = -\frac{3}{2}t_3\delta k_y^2 + \frac{\sqrt{3}}{2}t\delta k_y\delta k_x - t_3\delta k_x^2$, and $p_3(\delta\mathbf{k}) = -\frac{3}{4}(t-2t_3)\delta ky^2 - \frac{1}{4}(t-4t_3)\delta k_x^2$ are the quadratic contributions to the off-diagonal matrix elements that will play an important role in the self-consistent Born approximation used to study the disordered case. It is evident that the gap at all three $\mathbf{M}_a$ is given by $|t-3t_3|$, though the sign is different for the $\mathbf{M_3}$ point relative to the $\mathbf{M_1}$ and $\mathbf{M_2}$ points[74]. Note also that the gap is controlled by the terms proportional to τ^x in the basis of the two bands, rather than τ^z, as occurs in the Kane-Mele model where the gap closings are located at the K and K' points. This fact has important implications for how different types of disorder (bond and on-site) will renormalize the effective masses (gaps) at the low-energy points of the theory[46].

C. The DKM Model

Here we provide the Hamiltonian expression for the DKM model[41,42] and develop its effective low-energy theory. The DKM model is given by $H_{\rm DKM} = H_{\rm KM} + H_{t_d}$ where $H_{t_d} = \delta t_d \sum_{i\in A, j=i+\hat{e}_3,\sigma} c^\dagger_{i\sigma}c_{j\sigma}$ where we chose the dimerized bonds along the nearest neighbor $\hat{e}_3 = (\mathbf{e}_1+\mathbf{e}_2)/|\mathbf{e}_1+\mathbf{e}_2|$ direction. It can be expressed in momentum space as[74],

$$H_{DKM} = \sum_{\mathbf{k}\in B.Z.} \Psi^\dagger_{\mathbf{k}}\Bigg[\begin{pmatrix} 0 & -t_d - tf_d(\mathbf{k}) \\ -t_d - tf^*_d(\mathbf{k}) & 0 \end{pmatrix}\otimes \mathbb{1}_{2\times 2} + \begin{pmatrix} 2\lambda_{so}g(\mathbf{k}) & 0 \\ 0 & -2\lambda_{so}g(\mathbf{k}) \end{pmatrix}\otimes\sigma_z\Bigg]\Psi_{\mathbf{k}}, \tag{16}$$

where $f_d(\mathbf{k}) = e^{i\mathbf{k}\cdot\mathbf{e}_1} + e^{i\mathbf{k}\cdot\mathbf{e}_2}$. When we vary the dimerized hopping amplitude t_d while fixing t, the band gap only closes at $\mathbf{M}_3$ due to the breakdown of C_3 rotational

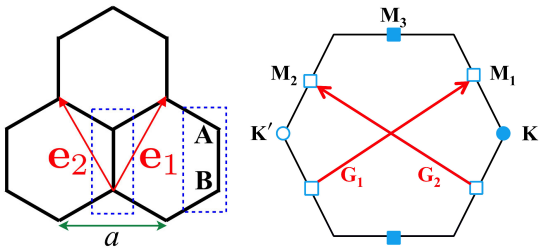

FIG. 1. (a) Schematic of the honeycomb lattice with two sublattices labeled A and B. The vectors $\mathbf{e}_{1/2} = (\pm 1/2, \sqrt{3}/2)$ connect the same sublattice in different unit cells. The lattice constant a is set to 1. (b) Illustration of the Brillouin zone (B.Z.). There are several relevant momenta that are important in the low-energy descriptions of variants of KM models–The usual momenta $\mathbf{K} = -\mathbf{K}' = (4\pi/3, 0)$ as the locations of the Dirac nodes in the original KM model and the time-reversal-invariant momenta (TRIM) $\mathbf{M}_{1,2} \equiv (\pm\pi, \pi/\sqrt{3})$ and $\mathbf{M}_3 \equiv (0, 2\pi/\sqrt{3})$. Note that $\mathbf{M}_1$ and $\mathbf{M}_2$ are related by C_3 lattice rotation symmetry. $\mathbf{G}_1$ and $\mathbf{G}_2$ are the reciprocal lattice vectors.

symmetry. Similar to the GKM, the band gap at the TRIM ($\mathbf{M}_3$) is controlled by the off-diagonal terms since $g(\mathbf{M}_3) = 0$. The low-energy form of the DKM Hamiltonian near $\mathbf{M}_3$ can be obtained from

$$f_d(\mathbf{M_3} + \delta\mathbf{k}) = -2 - i\sqrt{3}\delta k_y + \frac{3}{4}\delta k_y^2 + \frac{1}{4}\delta k_x^2, \qquad (17)$$

which yields

$$H^{eff}_{DKM}(\mathbf{M_3} + \delta\mathbf{k}) = \begin{pmatrix} 4\lambda\delta k_x & 2t - t_d + i\sqrt{3}t\delta k_y - \frac{1}{4}t(3\delta k_y^2 + \delta k_x^2) \\ 2t - t_d - i\sqrt{3}t\delta k_y - \frac{1}{4}t(3\delta k_y^2 + \delta k_x^2) & -4\lambda\delta k_x \end{pmatrix}, \qquad (18)$$

so that the gap at the $\mathbf{M}_3$ point is given by $|-t_d + 2t|$. Here, we have used the relation $t_d = t + \delta t_d$, so the modification of the KM model to the DKM model has an additional δt_d along the $\hat{e}_3$ direction.

III. NUMERICAL TECHNIQUES

A. Evaluation of the Chern numbers in the presence of disorder and interactions

Here we describe how to compute the Chern number of a generic projector P defined on the Hilbert space of a lattice Hamiltonian. We recall that the defining characteristics of a projection are $P^2 = P$ and $P^\dagger = P$. If the projector commutes with the translations, $[T_a, P] = 0$, then it accepts a Bloch-Floquet decomposition:

$$\langle \boldsymbol{x}|P|\boldsymbol{y}\rangle = \int_{\mathbb{T}^2} \frac{\mathrm{d}\boldsymbol{k}}{(2\pi)^2}\, e^{i\boldsymbol{k}\cdot(\boldsymbol{x}-\boldsymbol{y})}\, P_{\boldsymbol{k}}, \qquad (19)$$

or

$$P = \sum_{\boldsymbol{x},\boldsymbol{y}} \int_{\mathbb{T}^2} \frac{\mathrm{d}\boldsymbol{k}}{(2\pi)^2}\, e^{i\boldsymbol{k}\cdot(\boldsymbol{x}-\boldsymbol{y})}\, P_{\boldsymbol{k}}|\boldsymbol{x}\rangle\langle\boldsymbol{y}|, \qquad (20)$$

where each of the $P_{\boldsymbol{k}}$ is a finite dimensional projector of dimension equal to the number of orbitals per primitive cell. Furthermore, if the matrix elements $\langle \boldsymbol{x}|P|\boldsymbol{y}\rangle$ decay fast enough with the separation $\boldsymbol{x} - \boldsymbol{y}$, then $P_{\boldsymbol{k}}$'s are smooth or even analytic functions of $\boldsymbol{k}$[34]. In this case, the Chern number[35]:

$$\mathrm{Ch}(P) = 2\pi\imath\epsilon^{\alpha\beta} \int_{\mathbb{T}^2} \frac{\mathrm{d}\boldsymbol{k}}{(2\pi)^2}\, \mathrm{tr}\big(P_{\boldsymbol{k}}\, \partial_{k_\alpha} P_{\boldsymbol{k}}\, \partial_{k_\beta} P_{\boldsymbol{k}}\big), \qquad (21)$$

is well defined and takes only quantized values. Above, "tr" refers to the trace over the local orbital degrees of freedom. This expression can be written in real-space using Eq. (19):

$$\mathrm{Ch}(P) = -2\pi\imath\epsilon^{\alpha\beta}\mathcal{T}\big(P\,[P, X_\alpha][P, X_\beta]\big), \qquad (22)$$

where $\mathcal{T}$ refers to the trace per volume $\lim_{V\to\infty}\frac{1}{V}\mathrm{Tr}_V\{\cdot\}$, equal to $\int_{\mathbb{T}^2}\frac{\mathrm{d}\boldsymbol{k}}{(2\pi)^2}$ for translationally invariant systems, and $\boldsymbol{X}$ is the position operator. One remarkable fact is that Eq.(22) remains stable and quantized even in the presence of strong disorder when the spectral gap is closed, provided the matrix elements $\langle \boldsymbol{x}|P|\boldsymbol{y}\rangle$ continue to display a fast decay, more precisely if:

$$\sum_{\boldsymbol{y}\in\mathbb{Z}^2} |\boldsymbol{x} - \boldsymbol{y}|^2 \big|\langle \boldsymbol{x}|P|\boldsymbol{y}\rangle\big|^2 \leq \infty. \qquad (23)$$

This happens to be the case for the Fermi projector of a non-interacting model when the Fermi level is located in a mobility gap[36], that is, whenever the diagonal components of the conductivity tensor vanish.

In the present work we are dealing with both disordered non-interacting and disordered interacting systems. For the former, the topology is encoded in the

Fermi projection, which projects onto the one-particle states with eigen-energy below the Fermi level. When the interaction is present, the projector that encodes the topology can be obtained from the two-point imaginary time Green's function:

$$G(\boldsymbol{x},\boldsymbol{y};\tau)=\langle\Psi_0|c^\dagger_{\boldsymbol{x}}(\tau)c_{\boldsymbol{y}}(0)|\Psi_0\rangle, \tag{24}$$

at zero frequency, as detailed in[54]. Its matrix elements will be obtained from Monte-Carlo simulations and the inverse of the resulting matrix plays the role of the one-particle Hamiltonian in non-interacting models. The equivalent of the Fermi projection is then obtained by filling the positive eigenvalues of this pseudo Hamiltonian. We define the topological invariant as the Chern number of this projector.

To evaluate Eq.(22), we follow the practical solution devised in the series of works[38–40]. The most difficult part of the problem is to represent or approximate the commutators $[X_j, F_\omega]$ for a disordered operator F_ω on a finite volume with periodic boundary conditions. Here, ω represents the disorder configuration and encodes all the random fluctuations in the Hamiltonian coefficients. Recall that on the infinite volume:

$$\langle\boldsymbol{x}|[X_j,F_\omega]|\boldsymbol{y}\rangle=(x_j-y_j)\langle\boldsymbol{x}|F_\omega|\boldsymbol{y}\rangle,\quad j=1,2, \tag{25}$$

and clearly the factor $x_j - y_j$ is antagonistic to the periodic boundary conditions. But there is a set of key observations:

- Typically, the kernels $\langle\boldsymbol{x}|F_\omega|\boldsymbol{y}\rangle$ decay exponentially with $|\boldsymbol{x}-\boldsymbol{y}|$, on average.
- When restricting $\boldsymbol{x}$ to a finite lattice $-N\leq x_j\leq N$, $j=1,2$, and imposing periodic boundary conditions, we are practically placing the system on the torus $\mathcal{C}_N\times\mathcal{C}_N$, where $\mathcal{C}_N$ is the circle of perimeter $2N+1$.
- The factor $x_j - y_j$ is indeed antagonistic to this circle but we only need to represent this factor exactly for $\boldsymbol{x}$ close to $\boldsymbol{y}$, which leaves plenty of room to make it compatible with the circle (i.e. periodic).

Based on these guiding principles, the following procedure was proposed in Ref. [40]. Let $f:[-1,1]\to\mathbb{R}$ be a smooth and periodic function such that $f(r)=r$, for $|r|$ smaller than some $\alpha\lesssim 1$. It is used to define a function on the circle $\mathcal{C}_N$: $f_N(x)=Nf(x/N)$, which has the correct periodicity and is equal to x for $|x|<\alpha N$. Let us consider its discrete Fourier representation:

$$f_N(x)=\frac{1}{2N+1}\sum_\lambda c_\lambda\lambda^x, \tag{26}$$

where the sum is over all $2N+1$ solutions of the equation $z^{2N+1}=1$. This will enable us to extend the domain of this function indefinitely (note that this is indeed needed because $x_j - x'_j$ takes values in the interval $[-2N, 2N]$) and to finally define the proper replacement of the antagonistic factor in Eq. (25):

$$x_j-y_j\to\sum_\lambda c_\lambda\lambda^{x_j-y_j}. \tag{27}$$

From the above approximation, a concrete form of the approximating commutators can be derived. Numerically, we found that the periodicity of the starting function f is not that important in practice, and in most of our calculations we simply use $f(r)=r$ over the entire $[-1,1]$ interval. In this case, the Fourier coefficients are known explicitly and given below.

To summarize, the canonical and optimal finite-volume approximation scheme that emerges from the above arguments consists of substituting the commutator $[X_j, F_\omega]$ with:

$$\lfloor X_j,\widetilde{F}_\omega\rfloor=\sum_{\lambda\neq1}c_\lambda\lambda^{X_j}\widetilde{F}_\omega\lambda^{-X_j},\quad c_\lambda=\frac{\lambda^{N+1}}{1-\lambda}, \tag{28}$$

where $\widetilde{F}_\omega$ represents the finite-volume approximation of F_ω. Based on the key factors listed above, Ref. [40] established the following rigorous result. Let Φ_j be smooth functions and let the tilde $\sim$ indicate the restriction to a finite volume. Then:

$$\begin{aligned}&\big|\mathcal{T}\{[X_{\alpha_1},\Phi_1(F_\omega)][X_{\alpha_2},\Phi_2(F_\omega)]\ldots\}\\&-\widetilde{\mathcal{T}}\{\lfloor X_{\alpha_1},\Phi_1(\widetilde{F}_\omega)\rfloor\lfloor X_{\alpha_2},\Phi_2(\widetilde{F}_\omega)\rfloor\ldots\}\big|<C_\Phi e^{-\gamma N}.\end{aligned} \tag{29}$$

Based on this result, any correlation function involving localized observables and their commutators with the position operators can be canonically approximated on a finite volume, and this approximation converges exponentially fast to the thermodynamic limit. This is the key feature which makes the Chern number calculations possible for the interacting case, because the quantization can be achieved on relatively small volumes.

B. Quantum Monte-Carlo Calculations

We use the quantum Monte Carlo techniques as described in Ref.[41,42,54,74] to compute the single-particle Greens in real space for each disorder realization. From the zero frequency real-space Greens' function, we use the results from the first section of the supplemental material to obtain a highly accurate value for the spin-Chern number. In our calculations, for each interaction value U, we used between 10 and 30 disorder realizations on a 12×12 lattice. Smaller 6×6 sizes could not give accurate results, and 18×18 was beyond our computational capability.

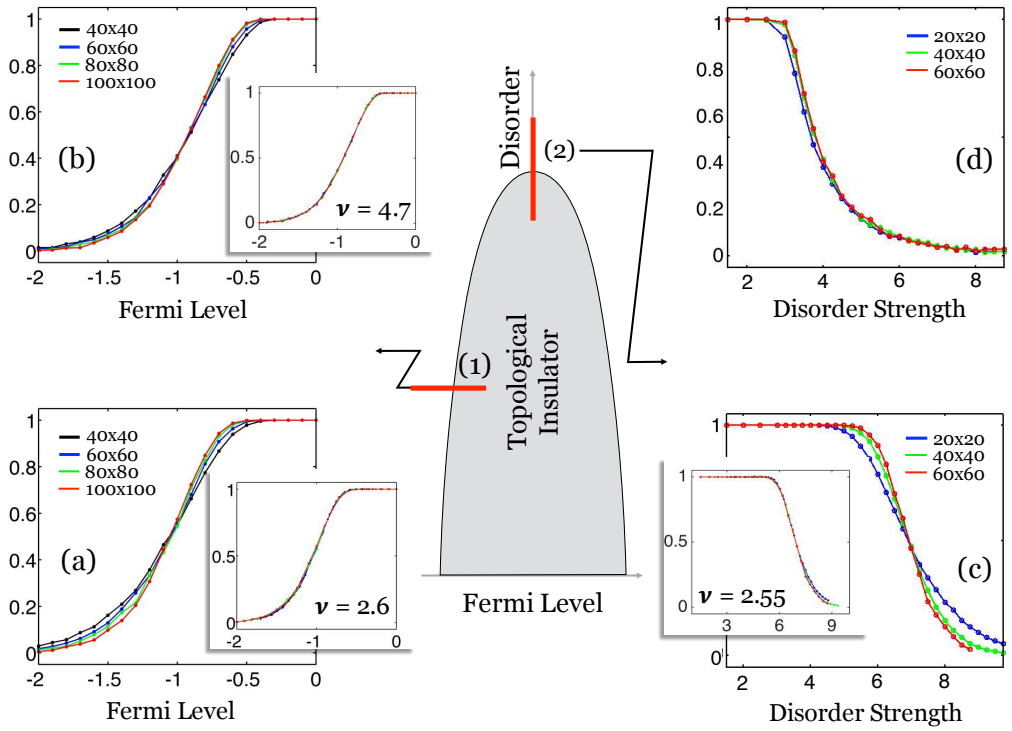

FIG. 2. Exact diagonalization study of the Kane-Mele model, Eq.(1), with bond [panels (a) and (c)] and on-site [panels (b) and (d)] disorder. The center of the figure shows a qualitative representation of the phase diagram, with a topological phase Ch = 1 (spin Chern number) trapped inside (gray region) an infinitely thin phase boundary. On the other side of the phase boundary, there is a trivial insulator Ch = 0. For bond-disorder there is an exception at the top of the phase diagram, along the vertical axis, where a metallic phase is stabilized by the particle-hole symmetry. The panels show the evolution of the Chern number along the phase-boundary crossings indicated on the diagram. The various curves in the main panels correspond to different lattice sizes and the insets demonstrate the single-parameter scaling of the data, fit to Eq.(30) for panels (a) and (b), and Eq.(31) for panel (c). Case (d) is a transition from an insulating to a metallic state. For further details, see text.

IV. NUMERICAL RESULTS

A. Non-interacting Models

Fig. 2 qualitatively illustrates a phase diagram of the disordered Kane-Mele model, Eq.(1), and the evolution of the Chern number for the spin-up sector, as the model transits the phase boundary. We study two types of disorder, on-site disorder $H_{\rm on-site} = \sum_i \omega_i n_i$ and bond-disorder $H_{\rm bond} = \sum_{\langle i,j\rangle,\sigma} \omega_{ij} c^\dagger_{i\sigma} c_{j\sigma}$, which were separately added to the KM model. In both cases, the ω's are independent random variables drawn uniformly from the interval $[-W/2, W/2]$, with W representing the disorder strength. In Fig. 2, $t = 1$ and $\lambda_{SO} = 0.3$.

Since the z-component of the spin is conserved, effectively the disordered models belong to the universality class A[51]. In this case, the phase boundary consists of an infinitely thin line where the localization length diverges[39]. At half-filling with the bond-disorder, the model displays an exact particle-hole symmetry which changes the universality class to D[51] and qualitatively modifies the phase diagram. In this case the system will cross into a metallic phase[52] (similar behavior has been observed for other types of disorder[53]). This strict preservation of the particle-hole symmetry is important for quantum Monte Carlo calculations because the fermion sign-problem can be avoided[41,42,54].

The crucial point of the computations reported in Fig. 2 is to exemplify a procedure, based on the finite-size critical scaling behavior, for the precise identification of the phase boundary[55]. To accurately compute the topological invariant, we make use of recent advances in the real-space evaluation of the Chern number, which exhibits exponential convergence when the lattice size exceeds the Anderson localization length. As the critical boundary is approached, the localization length will exceed any lattice size, hence even with these fast converging algorithms one cannot obtain a sharp stepping profile of the topological invariants. There will be a sizable region where the value of the topological invariants (of the infinite system) cannot be determined numerically. Nevertheless, the invariants obey finite-size critical scaling behavior which effectively locates the true critical

phase boundary and determines critical exponents. We averaged over 100 disorder realizations.

In panels (a) and (b), the phase boundary is traversed as indicated by the red segment (1), hence varying the Fermi level while keeping the disorder strength fixed. Panel (a) corresponds to the on-site disorder of strength $W = 4$ while panel (b) to the bond-disorder of strength $W = 3$, a lower value because the effect of disorder is stronger in this case [compare panels (c) and (d)]. The Chern number was evaluated on finite lattices of increasing sizes; the quantization and the transition between the quantized values becomes sharper as the lattice size is increased. The most important feature is intersection of the curves at a single point, signaling the existence of a unique critical point, E_F^c, separating two insulating phases. In the insets, we show that, upon the rescaling

$$E_F \to X = E_F^c + (E_F - E_F^c)\Big(\frac{L}{L_0}\Big)^{\frac{1}{\nu}}, \qquad (30)$$

the curves collapse on top of each other. The optimal collapse is obtained for $E_F^c = -1.00 \pm 0.01$ and $\nu = 2.6 \pm 0.1$ in the case of on-site disorder, and $E_c = -0.98 \pm 0.01$ and $\nu = 4.7 \pm 0.01$ in the case of bond-disorder. Note that the value $\nu = 2.6$ is in very good agreement with the numerical values reported in the literature[56–62].

In panels (c) and (d), the phase boundary is traversed as indicated by the red segment (2), by varying the the disorder strength while keeping the Fermi level fixed at $E_F = 0$ (half-filling). In panel (c), the curves intersect each other at a single point indicating again the existence of a unique critical point E_F^c separating two insulating phases. In the insets, we show that, upon the rescaling

$$W \to X = W^c + (W - W^c)\Big(\frac{L}{L_0}\Big)^{\frac{1}{\nu}}, \qquad (31)$$

the curves collapse on top of each other. The optimal collapse is obtained for $W^c = 6.75 \pm 0.01$ and $\nu = 2.55$, with the small differences in the critical exponent from case (a) attributed to the smaller lattices in the simulations.

Panel (d), which corresponds to the bond-disorder in the particle-hole symmetric case, looks markedly different from the previous panels. Here, the curves decay to zero without intersecting each other at a unique critical point. On the large W side, there is little variation of the curves from one system-size to another, an indicative that the system entered a metallic phase (that vanishes as soon as particle-hole symmetry is broken). The scaling analysis should apply over the insulating side of the phase diagram, but it was difficult to perform in this case and we omitted it in Fig. 1. Nevertheless, the analysis indicates that the critical point, which marks the phase boundary between the topological insulator and metallic phase, is located very close to the point where the graphs start to deviate from the quantized value of 1.

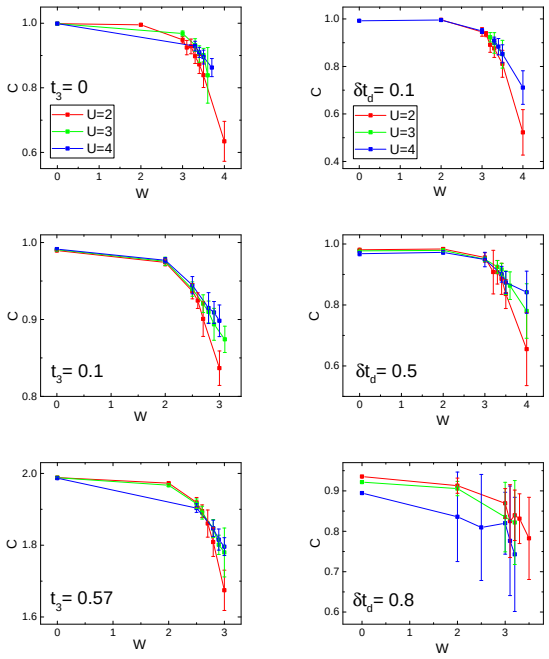

FIG. 3. QMC calculations for spin Chern numbers at different interaction strengths, $U = 2, 3, 4$. Between 10 and 30 disorder realizations are averaged over. The top panels show the disorder dependence of the spin Chern number for different values of the one-body tuning parameter t_3 for the GKMH model, and the bottom panels show the disorder dependence of the spin Chern number for different values of the one-body tuning parameter δt_d for the DKMH model.

B. Interacting Models

We study two generalizations of the Kane-Mele-Hubbard (KMH) model, $H_{\rm KMH} = H_{\rm KM} + H_U$[63–72]: (1) the generalized KMH (GKMH) model and (2) the dimerized KMH (DKMH) model. In the absence of disorder, both models are already well characterized by QMC[41,42], dynamical mean-field theory[73], and analytical methods[74,75], setting a solid starting point for investigating the effects of disorder on interacting topological systems.

A critical difference between the KM model and the non-interacting GKM and DKM models is that that gap closings occur at the **M** points of the Brillouin zone in the latter two, while it occurs at the **K** and **K′** points in the former. This has important consequences for how the bond and the on-site disorders influence the phase transitions in the GKM and DKM models. In particular, for models with a gap closing at the **K** and **K′** points, bond disorder and on-site disorder lead to different signs of contributions to the gap[46]. By contrast, when the gap closings are at the **M** points, bond disorder and on-site disorder lead to the same sign of contribution to the gap. Therefore, one expects qualitatively similar results for the disordered GKMH and DKMH models regardless of

whether one studies bond disorder or on-site disorder, so we make use of the fact that we can simulate the former in QMC without a sign problem.

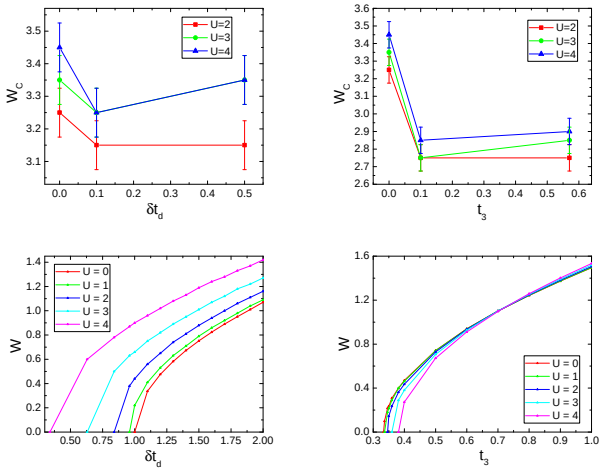

FIG. 4. **Top Panels:** Influence of disorder and interactions on the phase diagram of the DKM and GKM models computed within QMC. The critical disorder strength is determined by analyzing the disorder averaged spin Chern number. **Bottom Panels:** Influence of disorder and interactions on the phase diagram of the DKMH and GKMH models computed using the self-consistent Born approximation (SCBA). The curves represent the critical phase boundaries for various values of U separating the Z_2 topological/trivial phases, located in the upper/lower regions, respectively. Disorder tends to stabilize the topological phases. Interactions tend to destabilize the topological phase in the DKMH model and stabilize it in the GKMH model.

In the non-interacting limit of the GKMH model, t_3 drives a quantum phase transition at $t_3 = 1/3$, with a topological insulator with spin Chern number ± 1 for $0 < t_3 < 1/3$ and a trivial insulator for $t_3 > 1/3$ with spin Chern number ∓ 2[41,42]. In the non-interacting limit of the DKMH model, δt_d drives a topological phase transition at $\delta t_d = 1$, with spin Chern number ± 1 for $0 < \delta t_d < 1$ and a trivial insulator for $\delta t_d > 1$ with spin Chern number 0[41,42]. The one-body parameters t_3 and δt_d also drive a quantum phase transition at finite Hubbard U (for U below the critical value for a magnetic transition, as we consider in this work[41,42,73–75]), though the critical values of t_3 and δt_d generally depend on the strength of the interaction[41,42,73–75].

Our main results are shown in Fig. 3. We use these results to determine the critical disorder strength, W_c, for each model using a "peel off" criterion: When the Chern number decreases by 10% with respect to the $W = 0$ limit, this value is identified as the critical disorder strength for that particular value of U and t_3 or δt_d. These critical values for the two models are summarized in the top panel of Fig.4. For the GKMH model there is a quantum phase transition near $t_3 = 1/3$ (the critical t_3^c depends on the U value, as shown in the lower panel of Fig.4), where the spin Chern number in the clean limit changes from 1 for $0 < t_3 < t_3^c$ to 2 for $t_3 > t_3^c$. This is evident in the figures in the upper panel of Fig.3. For the DKMH there is quantum phase transition near $\delta t_d = 1$ (the critical δt_d^c depends on the U value, as shown in the lower panel of Fig.4, where the spin Chern number in the clean limit changes from 1 for $0 < \delta t_d < \delta t_d^c$ to 0 for $\delta t_d > \delta t_d^c$. Since there is no transition with disorder in the spin Chern number for $\delta t_d > \delta t_d^c$ we do not consider this case. Note that near the transition, where $\delta t_d = 0.8$, the fluctuations in the spin Chern number are large. This prevents us from an accurate determination of the critical value of W near phase boundaries. In addition, our inability to compute larger size lattices also prevents a finite scaling analysis that would help provide a more accurate W_c in the thermodynamic limit.

The phase diagrams derived from Fig. 3 are shown in Fig. 4. In the top panels, the critical disorder strength to drive the spin Chern number for each value of $U, t_3/\delta t_d$ to zero is shown. These computationally demanding results make use of highly accurate real-space Chern number evaluation, but can only be performed for one "large" lattice size, preventing a finite-size scaling analysis and smaller error bars. Overall, the trend is that larger interactions tend to lead to a larger W_c, which is consistent with the SCBA in the lower panels, for much of the parameter space. An important result to emerge from the SCBA in the lower panels is that disorder tends to stabilize the TI state which lives "above" the curves in the lower panel, consistent with analytical arguments.

V. THEORETICAL ANALYSIS

We also analyzed the disordered GKMH and DKMH models system using the self-consistent Born approximation (SCBA)[46–49]. We are interested in exploring the interplay of topology, interactions, and disorder on an equal footing. The QMC calculations are most stable for moderate interaction strengths, U, but we are able to analytically study the weak interaction limits using perturbation theory (in the interactions) combined with mean-field theory to obtain a renormalized band structure[74,75] that is used in the SCBA. Prior work has shown that (i) in the weak disorder limit, the SCBA provides a high level of quantitative agreement with exact diagonalization studies[47], and (ii) our pertubation+mean-field theory works semi-quantitatively well when compared to QMC[74,75]. We therefore combine the two to provide an analytical theory of combined disorder and interaction effects in topological insulators, generally applicable to any model, regardless of whether it can be simulated with fermion sign-free QMC, or the spatial dimension.

A. Self-consistent Born approximation (SCBA)

We follow the notation of Refs.[46,47]. In contrast to earlier studies[46–49] of disordered models with topological phases that had gap closings at either the Γ point or the K, K' points, the GKM model has gap closings at the three $\mathbf{M_a}$ points[41,42], and the DKM model at the $\mathbf{M_3}$ point[42,74]. As described in the section above, when the Hamiltonian is written in the basis (for a fixed spin orientation) of $H_0(\mathbf{k}) = h_0(\mathbf{k})\tau_0 + h_x(\mathbf{k})\tau_x + h_y(\mathbf{k})\tau_y + h_z(\mathbf{k})\tau_z$, it is the τ_x component that controls the gap. In the SCBA the (momentum-independent) self-energy, Σ, is computed from

$$\Sigma(E^+) = \frac{W^2}{12}\left(\frac{a}{2\pi}\right)^2 \int_{\rm BZ} d^2k \left[\tau_d (E^+\mathbb{1} - H_0 - \Sigma(E^+))^{-1}\tau_d\right], \tag{32}$$

where $E^+ = E_F + i\eta$ with $\eta > 0$ an infinitesimal, W is the width of the random portion of the one body terms drawn from $[-W/2, W/2]$, and $\tau_d = \tau_x$ if the disorder is on the hopping terms and $\tau_d = \tau_0$ if the disorder is on-site[46], as in the conventional study of Anderson localization.

As pointed out in Ref.[46], if the mass gap is controlled by τ_z as it is at the Γ point or the K, K' points, then hopping and on-site disorder terms have a contribution of opposite sign to the self-energy since $\tau_x\tau_z\tau_x = -\tau_z$, while $\tau_0\tau_z\tau_o = +\tau_z$. However, if the mass gap is controlled by the τ_x piece of H_0 as it is for the GKM and DKM models: $H_0(\mathbf{M_a}) = M\tau_x$, then hopping and on-site disorder have a contribution of the same sign since $\tau_x\tau_x\tau_x = +\tau_x$ and $\tau_0\tau_x\tau_0 = +\tau_x$, a new feature of the GKM and DKM models compared to earlier studies. The mass at the $\mathbf{M_a}$ points are then renormalized as,

$$\bar{M} = M + \Sigma_x(E = 0^+), \tag{33}$$

and the chemical potential is renormalized as

$$\mu = E_F - \Sigma_0(E = 0^+). \tag{34}$$

Approximate forms[46,47] for the renormalized mass gap and chemical potential can be found by neglecting the self-energy in the integrand on the right-hand side of Eq.(32),

$$\Sigma(E^+) \approx \frac{W^2}{12}\left(\frac{a}{2\pi}\right)^2 \int_{\rm BZ} d^2k \left[\tau_d (E^+\mathbb{1} - H_0)^{-1}\tau_d\right]. \tag{35}$$

For a given spin projection, the Hamiltonian matrix H_0 is 2×2, so that we may write (for $h_0(\mathbf{k}) \equiv 0$, as is appropriate for our models),

$$(E^+\mathbb{1} - H_0)^{-1} = \frac{1}{(E^+)^2 - \vec{h}(\mathbf{k})\cdot\vec{h}(\mathbf{k})}\left(E^+\mathbb{1} + H_0\right), \tag{36}$$

where $\vec{h}(\mathbf{k}) = (h_x(\mathbf{k}), h_y(\mathbf{k}), h_z(\mathbf{k}))$. Thus, an approximate form for the mass and chemical potential contributions to the self-energy are,

$$\Sigma_x(E^+) \approx +\frac{W^2}{12}\left(\frac{a}{2\pi}\right)^2 \int_{\rm BZ} d^2k \frac{h_x(\mathbf{k})}{(E^+)^2 - \vec{h}(\mathbf{k})\cdot\vec{h}(\mathbf{k})}, \tag{37}$$

and

$$\Sigma_0(E^+) \approx +\frac{W^2}{12}\left(\frac{a}{2\pi}\right)^2 \int_{\rm BZ} d^2k \frac{E^+}{(E^+)^2 - \vec{h}(\mathbf{k})\cdot\vec{h}(\mathbf{k})}, \tag{38}$$

where the expressions Eq.(37) and Eq.(38) are independent of whether $\tau_d = \tau_0$ for on-site disorder, or $\tau_d = \tau_x$ for hopping disorder. From the low-energy expression of the GKM model, Eq.(13), Eq.(14), Eq.(15), and the DKM model, Eq.(18), we have $E^+ = 0$ for a half-filled particle-hole symmetric state. Hence, $\Sigma_0(E^+ = 0) \equiv 0$ and the chemical potential is *not* renormalized, according to Eq.(34).

We thus focus on the mass renormalization due to the disorder potential in the particle-hole symmetric state,

$$\Sigma_x(E^+ = 0^+) \approx -\frac{W^2}{12}\left(\frac{a}{2\pi}\right)^2 \int_{\rm BZ} d^2k \frac{h_x(\mathbf{k})}{\vec{h}(\mathbf{k})\cdot\vec{h}(\mathbf{k}) - (0^+)^2}, \tag{39}$$

which has its dominant contributions around $\mathbf{k}$ values where the denominator is smallest–namely around the $\mathbf{M_a}$ points. For both the GKM and the DKM models, the Hamiltonian is proportional to τ_x alone (at the $\mathbf{M_a}$ points), so if we neglect the momentum dependence of $h(\mathbf{k})$ and set it equal to the mass M, then we have $\Sigma(E^+ = 0^+)_x \approx -\frac{W^2}{12}\left(\frac{a}{2\pi}\right)^2 \int_{\approx \mathbf{M_a}} d^2k \frac{1}{M}$ which will have the opposite sign as M itself. However, one is not guaranteed that the integral is dominated by $\mathbf{k} \approx 0$. It turns out that the momentum dependence of $\vec{h}(\mathbf{k})$ is critical to obtain a the correct sign of the mass renormalization. In particular, it is the quadratic dependence contained in the functions $p_1(\mathbf{k}), p_2(\mathbf{k}), p_3(\mathbf{k})$ [see Eqs.(13)-(15)] and the quadratic terms proportional to τ_x in Eq.(18) that are responsible for the sign changes of the masses around any particular $\mathbf{M_a}$ point.

Provided there is a mass gap around each of the $\mathbf{M_a}$ points, one can neglect the $(0^+)^2$ in Eq.(39) so that the denominator of the integrand is manifestly positive. The correct sign of $\Sigma_x(E^+ = 0^+)$ relative to M will come from $h_x(\mathbf{k})$, and the structure of the low-energy form of the GKM and DKM Hamiltonians implies it is the quadratic terms that are critical for obtaining the correct sign change. Unfortunately, because the dispersions around the $\mathbf{M_a}$ points are not isotropic, it is not possible to obtain simple closed analytical forms (for general parameters) for the leading corrections to Σ_x as could be done for the Bernevig-Hughes-Zhang model[47] or the Kane-Mele model[46]. However, in special cases, closed analytical forms are available.

Around the $\mathbf{M_3}$ point the DKM model can be written as $H^{eff}_{DKM}(\mathbf{k}) = [(2t - t_d) - \frac{1}{4}t(k_x^2 + 3k_y^2)]\tau_x - \sqrt{3}tk_y\tau_y +$

$4\lambda k_x \tau_z$, so that the integral in Eq.(39) may be written as

$$\Sigma_x(E^+ = 0^+) \approx -\frac{W^2}{12}\left(\frac{a}{2\pi}\right)^2 \int_{\approx \mathbf{M_3}} dk_x dk_y \frac{(2t - t_d) - \frac{1}{4}t(k_x^2 + 3k_y^2)}{[(2t - t_d) - \frac{1}{4}t(k_x^2 + 3k_y)^2]^2 + 16\lambda^2 k_x^2 + 3t^2 k_y^2}, \tag{40}$$

which can be simplified by rescaling $\tilde{k}_y = \sqrt{3}k_y$ and choosing $\lambda = t/2$ (in our numerical calculations, we assumed $\lambda = .4t$) so that the integral becomes spherically symmetric,

$$\begin{aligned}\Sigma_x(E^+ = 0^+) \approx & \\ & -\frac{W^2}{12}\left(\frac{a}{2\pi}\right)^2 \frac{1}{\sqrt{3}} \int_{\approx \mathbf{M_3}} d^2k \frac{\alpha + \beta k^2}{\alpha^2 + \delta k^2 + \beta^2 k^4} \\ & \approx -\frac{W^2}{12}\left(\frac{a}{2\pi}\right)^2 \frac{2\pi}{2\sqrt{3}} \int_0^{\pi\hbar/a} du \frac{\alpha + \beta u}{\alpha^2 + \delta u + \beta^2 u^2},\end{aligned} \tag{41}$$

where $\alpha = (2t - t_d), \beta = -t/4$, and $\delta = tt_d/2$. This then gives a leading logarithmic contribution of

$$\Sigma_x(E^+ = 0^+) \approx -\frac{W^2 a^2}{24\sqrt{3}\pi} \frac{1}{\beta} \log\left|\frac{\beta^2}{\alpha^2}\left(\frac{\pi\hbar}{a}\right)^4\right|. \tag{42}$$

The mass gap is $M = \alpha = (2t - t_d)$, which then always has a *positive* contribution since $\beta < 0$. Since the topological phase of the DKM model has $\alpha = (2t - t_d) > 0$, the disorder always tends to *stabilize* the topological phase, and may even drive a trivial state with $2t < t_d$ into a topological state, as our numerical calculations show. Our numerical calculations are based on a fully self-consistent numerical solution of Eq.(32).

For the GKM model the self-energy cannot generally be cast into the form of Eq.(41) (even for special parameter values), though the physics is essentially the same as an in the DKM model. Critically, the effect of the disorder is to drive all three mass terms (at the three $\mathbf{M_a}$ points) to change their sign in the direction of the topological phase, regardless of whether the parameters in the clean limit put the Hamiltonian in the topological or trivial phase. Our numerical calculations for the GKM are also based on a fully self-consistent numerical solution of Eq.(32), and are shown in the bottom panels of Fig.4.

VI. SIMULTANEOUS TREATMENT OF INTERACTIONS AND DISORDER (PERTURBATIVE)

In our work, we perform Monte Carlo simulations of interacting, disordered, fermion-sign problem free models (DKMH and GKMH models) with Z_2 topological insulator phases in their phase diagrams. We were interested in exploring the interplay of topology, interactions, and disorder on an equal footing. The QMC calculations are most stable for moderate interaction strengths, U, but we are able to analytically study the weak interaction limits using perturbation theory (in the interactions) combined with mean-field theory to obtain a renormalized band structure[74,75].

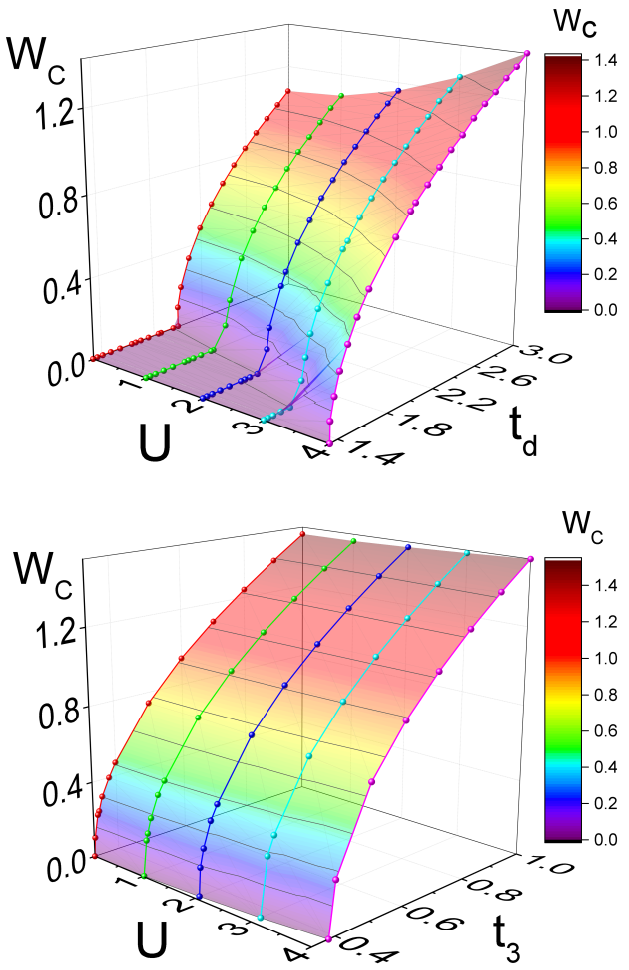

FIG. 5. Influence of disorder and interactions on the phase diagram of the DKM and GKM models computed using the self-consistent Born approximation (SCBA), Eq.(46) and Eq.(43). The region "above" the surface is a Z_2 topological insulator, and the region "below" it is a trivial insulator.

In Refs.[74,75], it was shown that the parameters of the

GKMH model are renormalized as

$$t \to t + U^2(\chi_1)^3, \tag{43}$$
$$t_3 \to t_3 + U^2(\chi_3)^3, \tag{44}$$
$$\tag{45}$$

where χ_1 is the expectation value of the nearest neighbor hopping in the presence of interactions, and χ_3 is the expectation value of the third neighbor hopping in the presence of interactions. This leads to a renormalized gap of $\Delta_G = t - 3t_3 + U^2((\chi_1)^3 - 3(\chi_3)^3)$. For $t \approx 3t_3$, one has $\chi_1 = 0.20705$ and $\chi_3 = 0.03064$, so that the correction to the gap is $0.00879U^2$. The positive sign of this term tends to stabilize the topological state[74,75].

In Refs.[74,75], it was shown that the parameters of the DKMH model are renormalized as

$$t \to t + U^2(\chi_1)^3, \tag{46}$$
$$t_d \to t_d + U^2(\chi_1^d)^3, \tag{47}$$
$$\tag{48}$$

where χ_1 is the expectation value of the nearest neighbor hopping in the presence of interactions, and χ_1^d is the expectation value of the modified first neighbor hopping in the presence of interactions. This leads to a renormalized gap of $\Delta_D = 2t - t_d - U^2((\chi_1^d)^3 - 2(\chi_1)^3)$. For $t \approx 2t_d$, one has $\chi_1 = 0.15770$ and $\chi_1^d = 0.36627$, so that the correction to the gap is $-0.04129U^2$. The negative sign of this term tends to destabilize the topological state[74,75].

VII. CONCLUSIONS

In this work we have studied the interplay of disorder and interactions in two-dimensional lattice models that exhibit a topological insulator state. In addition, we have also used recent advances in the real-space numerical evaluation of topological invariants to accurately compute the scaling behavior across the phase boundaries of the disordered Kane-Mele model. The values of the critical exponents agree with theoretical expectations. Bond and on-site disorder were contrasted, which exhibited different scaling exponents in the Kane-Mele model, see Fig. 2.

For disordered interacting models, we studied two generalizations of the Kane-Mele-Hubbard model–both of which preserve particle-hole symmetry at half-filling, even when bond disorder is included. A fermion sign problem-free QMC study was compared with a perturbative (in disorder and interaction strength) self-consistent Born approximation, see Fig. 4. To within the numerical uncertainties of the QMC, there is agreement in the trends. Moreover, the extended (for interactions) SCBA can be applied to study the interplay of disorder and interactions in a completely general context, independent of spatial dimension and model symmetries.

An important feature of the generalized Kane-Mele models we study is that the gap closing is not at the $\mathbf{K}$ and $\mathbf{K}'$ points (or the $\mathbf{\Gamma}$ point) of the Brillouin zone, but rather the $\mathbf{M}$ points, which essentially presents a new class of models where disorder can be studied along with interactions. The gap closings at the $\mathbf{M}$ points implies that on-site and bond disorder will have the same effect on the sign of the gaps near the gap closing points, in contrast to other models in the literature. We hope this work will stimulate further theoretical and experimental study on disordered, interacting, topological systems.

Acknowledgements. E.P. acknowledges support from U.S. NSF grant DMR-1056168. G.A.F. acknowledges support from ARO grant W911NF-14-1-0579 and NSF DMR-1507621.

[1] J. E. Moore, Nature **464**, 194 (2010).
[2] M. Z. Hasan and C. L. Kane, Rev. Mod. Phys. **82**, 3045 (2010).
[3] X. L. Qi and S. C. Zhang, Rev. Mod. Phys. **83**, 1057 (2011).
[4] Y. Ando, J. Phys. Soc. Jpn. **82**, 102001 (2013).
[5] J. Maciejko and G. A. Fiete, Nat. Phys. **11**, 385 (2015).
[6] A. Stern, "Fractional topological insulators – a pedagogical review," (2015), arXiv:1509.02698.
[7] W. Witczak-Krempa, G. Chen, Y. B. Kim, and L. Balents, Annu. Rev. Condens. Matter Phys. **5**, 57 (2014).
[8] A. Mesaros and Y. Ran, Phys. Rev. B **87**, 155115 (2013).
[9] X. Chen, Z.-C. Gu, Z.-X. Liu, and X.-G. Wen, Phys. Rev. B **87**, 155114 (2013).
[10] A. Girschik, F. Libisch, and S. Rotter, Phys. Rev. B **91**, 214204 (2015).
[11] D. Xu, J. Qi, J. Liu, V. Sacksteder, X. C. Xie, and H. Jiang, Phys. Rev. B **85**, 195140 (2012).
[48] H. Jiang, L. Wang, Q.-F. Sun, and X. C. Xie, Phys. Rev. B **80**, 165316 (2009).
[46] J. Song, H. Liu, H. Jiang, Q.-F. Sun, and X. C. Xie, Phys. Rev. B **85**, 195125 (2012).
[49] J. Li, R.-L. Chu, J. K. Jain, and S.-Q. Shen, Phys. Rev. Lett. **102**, 136806 (2009).
[47] C. W. Groth, M. Wimmer, A. R. Akhmerov, J. Tworzydło, and C. W. J. Beenakker, Phys. Rev. Lett. **103**, 196805 (2009).
[16] E. Prodan, Phys. Rev. B **83**, 195119 (2011).
[17] H.-M. Guo, G. Rosenberg, G. Refael, and M. Franz, Phys. Rev. Lett. **105**, 216601 (2010).
[18] E. Prodan, T. L. Hughes, and B. A. Bernevig, Phys. Rev. Lett. **105**, 115501 (2010).
[19] M. Imada, A. Fujimori, and Y. Tokura, Rev. Mod. Phys. **70**, 1039 (1998).
[20] P. A. Lee, N. Nagaosa, and X. G. Wen, Rev. Mod. Phys. **78**, 17 (2006).
[21] A. Georges, G. Kotliar, W. Krauth, and M. J. Rozenberg, Rev. Mod. Phys. **68**, 13 (1996).
[22] D. N. Basov, R. D. Averitt, D. van der Marel, M. Dressel, and K. Haule, Rev. Mod. Phys. **83**, 471 (2011).
[23] E. Dagotto, Rev. Mod. Phys. **66**, 763 (1994).

[43] C. L. Kane and E. J. Mele, Phys. Rev. Lett. **95**, 146802 (2005).
[44] C. L. Kane and E. J. Mele, Phys. Rev. Lett. **95**, 226801 (2005).
[41] H.-H. Hung, L. Wang, Z.-C. Gu, and G. A. Fiete, Phys. Rev. B **87**, 121113 (2013).
[42] H.-H. Hung, V. Chua, L. Wang, and G. A. Fiete, Phys. Rev. B **89**, 235104 (2014).
[28] V. Chua and G. A. Fiete, Phys. Rev. B **84**, 195129 (2011).
[39] E. Prodan, J. Phys. A: Math. Theor. **44**, 113001 (2011).
[30] F. D. M. Haldane, Phys. Rev. Lett. **61**, 2015 (1988).
[31] D. N. Sheng, Z. Y. Weng, L. Sheng, and F. D. M. Haldane, Phys. Rev. Lett. **97**, 036808 (2006).
[32] E. Prodan, Phys. Rev. B **80**, 125327 (2009).
[33] Z. Xu, L. Sheng, D. Y. Xing, E. Prodan, and D. N. Sheng, Phys. Rev. B **85**, 075115 (2012).
[34] M. Reed and B. Simon, *Methods of Modern Mathematical Physics. Vol II. Fourier Analysis, Self-adjointness* (Academic Press, New York, 1975).
[35] J. E. Avron, L. Sadun, J. Segert, and B. Simon, Comm. Math. Phys. **124**, 595 (1989).
[36] J. Bellissard, A. van Elst, and H. Schulz-Baldes, J. Math. Phys. **35**, 5373 (1994).
[54] Zi Yang Meng, Hsiang-Hsuan Hung, Thomas C. Lang, *The characterization of topological properties in Quantum Monte Carlo simulations of the Kane-Mele-Hubbard model*, Mod. Phys. Lett B **28**, 143001 (2014).
[38] T. H. E. Prodan and B. Bernevig, Phys. Rev. Lett. **105**, 115501 (2010).
[39] E. Prodan, J. Phys. A: Math. Theor. **44**, 113001 (2011).
[40] E. Prodan, Appl. Math. Res. Express AMRX **2013**, 176 (2013).
[41] H.-H. Hung, L. Wang, Z.-C. Gu, and G. A. Fiete, Phys. Rev. B **87**, 121113 (2013).
[42] H.-H. Hung, V. Chua, L. Wang, and G. A. Fiete, Phys. Rev. B **89**, 235104 (2014).
[43] C. L. Kane and E. J. Mele, Phys. Rev. Lett. **95**, 146802 (2005).
[44] C. L. Kane and E. J. Mele, Phys. Rev. Lett. **95**, 226801 (2005).
[74] H.-H. Lai and H.-H. Hung, International Journal of Modern Physics B **29**, 1530005 (2015).
[46] J. Song, H. Liu, H. Jiang, Q.-F. Sun, and X. C. Xie, Phys. Rev. B **85**, 195125 (2012).
[47] C. W. Groth, M. Wimmer, A. R. Akhmerov, J. Tworzydło, and C. W. J. Beenakker, Phys. Rev. Lett. **103**, 196805 (2009).
[48] H. Jiang, L. Wang, Q.-F. Sun, and X. C. Xie, Phys. Rev. B **80**, 165316 (2009).
[49] J. Li, R.-L. Chu, J. K. Jain, and S.-Q. Shen, Phys. Rev. Lett. **102**, 136806 (2009).
[75] H.-H. Lai, H.-H. Hung, and G. A. Fiete, Phys. Rev. B **90**, 195120 (2014).
[51] A. P. Schnyder, S. Ryu, A. Furusaki, and A. W. W. Ludwig, Phys. Rev. B **78**, 195125 (2008).
[52] V. Kagalovsky and D. Nemirovsky, *Universal Critical Exponent in Class D Superconductors*, Phys. Rev. Lett. **101**, 127001 (2008).
[53] E. V. Castro, M. P. Lopez-Sancho, and M. A. H. Vozmediano, Phys. Rev. B **92**, 085410 (2015).
[54] Zi Yang Meng, Hsiang-Hsuan Hung, Thomas C. Lang, *The characterization of topological properties in Quantum Monte Carlo simulations of the Kane-Mele-Hubbard model*, Mod. Phys. Lett B **28**, 143001 (2014).
[55] J. Priest, S. P. Lim, and D. N. Sheng, Phys. Rev. B **89**, 075110 (2014).
[56] T. O. K. Slevin, Phys. Rev. B **80**, 041304 (2009).
[57] B. Kramer, A. MacKinnon, T. Ohtsuki, and K. Slevin, Int. J. Mod. Phys. B **24**, 1841 (2010).
[58] H. Obuse, A. R. Subramaniam, A. Furusaki, I. A. Gruzberg, and A. W. W. Ludwig, Phys. Rev. B **82**, 035309 (2010).
[59] I. C. Fulga, F. Hassler, A. R. Akhmerov, and C. W. J. Beenakker, Phys. Rev. B **84**, 245447 (2011).
[60] J. P. Dahlhaus, J. M. Edge, J. Tworzydo, and C. W. J. Beenakker, Phys. Rev. B **84**, 115113 (2011).
[61] K. Slevin and T. Ohtsuki, Int. J. Mod. Phys.: Conference Series **11**, 60 (2012).
[62] H. Obuse, I. A. Gruzberg, and F. Evers, Phys. Rev. Lett. **109**, 206804 (2012).
[63] H.-Q. Wu, Y.-Y. He, Y.-Z. You, C. Xu, Z. Y. Meng, and Z.-Y. Lu, Phys. Rev. B **92**, 165123 (2015).
[64] M. Laubach, J. Reuther, R. Thomale, and S. Rachel, Phys. Rev. B **90**, 165136 (2014).
[65] J. Reuther, R. Thomale, and S. Rachel, Phys. Rev. B **86**, 155127 (2012).
[66] C. Griset and C. Xu, Phys. Rev. B **85**, 045123 (2012).
[67] D. Zheng, G.-M. Zhang, and C. Wu, Phys. Rev. B **84**, 205121 (2011).
[68] S.-L. Yu, X. C. Xie, and J.-X. Li, Phys. Rev. Lett. **107**, 010401 (2011).
[69] S. Rachel and K. Le Hur, Phys. Rev. B **82**, 075106 (2010).
[70] M. Hohenadler and F. F. Assaad, J. Phys. Cond. Matt. **25**, 143201 (2013).
[71] M. Hohenadler, Z. Y. Meng, T. C. Lang, S. Wessel, A. Muramatsu, and F. F. Assaad, Phys. Rev. B **85**, 115132 (2012).
[72] F. Parisen Toldin, M. Hohenadler, F. F. Assaad, and I. F. Herbut, Phys. Rev. B **91**, 165108 (2015).
[73] Y.-H. Chen, H.-H. Hung, G. Su, G. A. Fiete, and C. S. Ting, Phys. Rev. B **91**, 045122 (2015).
[74] H.-H. Lai and H.-H. Hung, International Journal of Modern Physics B **29**, 1530005 (2015).
[75] H.-H. Lai, H.-H. Hung, and G. A. Fiete, Phys. Rev. B **90**, 195120 (2014).